

The Crystal Structure of NAD(P)H Oxidase from *Lactobacillus sanfranciscensis*: Insights into the Conversion of O₂ into Two Water Molecules by the Flavoenzyme^{†,‡}

George T. Lountos,^{§,||} Rongrong Jiang,^{⊥,Δ} William B. Wellborn,^{⊥,◇} Tracey L. Thaler,[§] Andreas S. Bommarius,^{*,§,⊥} and Allen M. Orville^{*,§,#}

School of Chemistry and Biochemistry, School of Chemical and Biomolecular Engineering, and the Petit Institute for Bioengineering and Bioscience, Georgia Institute of Technology, Atlanta, Georgia 30332

Received April 10, 2006; Revised Manuscript Received June 8, 2006

ABSTRACT: The FAD-dependent NAD(P)H oxidase from *Lactobacillus sanfranciscensis* (*L.san*-Nox2) catalyzes the oxidation of 2 equivalents of either NADH or NADPH and reduces 1 equivalent of O₂ to yield 2 equivalents of water. During steady-state turnover only 0.5% of the reducing equivalents are detected in solution as hydrogen peroxide, suggesting that it is not released from the enzyme after the oxidation of the first equivalent of NAD(P)H and reaction with O₂. Here we report the crystal structure of *L.san*-Nox2 to 1.8 Å resolution. The enzyme crystallizes as a dimer with each monomer consisting of a FAD binding domain (residues 1–120), a NAD(P)H binding domain (residues 150–250), and a dimerization domain (residues 325–451). The electron density for the redox-active Cys42 residue located adjacent to the *si*-face FAD is consistent with oxidation to the sulfenic acid (Cys-SOH) state. The side chain of Cys42 is also observed in two conformations; in one the sulfenic acid is hydrogen bonded to His10 and in the other it hydrogen bonds with the FAD O2' atom. Surprisingly, the NAD(P)H binding domains each contain an ADP ligand as established by electron density maps and MALDI-TOF analysis of the ligands released from heat-denatured enzyme. The ADP ligand copurifies with the enzyme, and its presence does not inhibit enzyme activity. Consequently, we hypothesize that either NADPH or NADH substrates bind via a long channel that extends from the enzyme exterior and terminates at the FAD *re*-face. A homology model of the NADH oxidase from *Lactococcus lactis* (*L.lac*-Nox2) was also generated using the crystal structure of *L.san*-Nox2, which reveals several important similarities and differences between the two enzymes. HPLC analysis of ligands released from denatured *L.lac*-Nox2 indicates that it does not bind ADP, which correlates with the specificity of the enzyme for oxidation of NADH.

Lactobacillus sanfranciscensis and *Lactococcus lactis* are aerotolerant anaerobes and obligatory heterofermentative mi-

croorganisms (1). Genomic sequencing and analysis of several lactic acid bacteria suggest that most do not synthesize hemes or cytochromes (2–6). Consequently, they are unable to use an electron transport chain or oxidative phosphorylation and thus must satisfy all of their energy requirements with glycolysis. In the absence of heme-based oxidases or catalases, oxidative stress is managed in many lactic acid bacteria or other facultative and strict anaerobic bacteria by the expression of one or more flavin-dependent NAD(P)H oxidase(s) (2, 3, 7–12). Therefore, the NAD(P)H oxidases play important functional roles in regenerating oxidized pyridine nucleotides for glycolysis and to help protect the organisms from oxidative stress. Indeed, recent studies have shown that the NADH oxidases from *Archaeoglobus fulgidus*, *Streptococcus pyogenes*, *Streptococcus mutans*, and *Lactobacillus delbrueckii* contribute significantly to their aerobic metabolism under growth conditions that include oxidative stress (13–15).

Sequence analysis of these and the related NADH peroxidase enzymes reveals sequence identities with the NAD(P)H oxidase from *L. sanfranciscensis* (*L.san*-Nox2)¹ that range from 39% for the crystallographically defined NADH peroxidase from *Enterococcus faecalis* (NPX) (16), 23% for the putative NADH peroxidase from *S. pyogenes* MGAS315, and 59% for the NADH oxidase from *Lactobacillus plantarum* WCFS1 (17–19). In each case, the most highly conserved regions include either the redox-active cysteine

[†] This work was supported by the Georgia Tech Research Corporation, the Office of the Vice Provost for Research, Georgia Institute of Technology, an American Chemical Society Petroleum Research Fund type G grant (40310-G4), and an American Heart Association Grant in Aid (0555286B) to A.M.O. Support was provided to A.S.B. by the Georgia Tech Research Corporation and the Office of Vice Provost for Research. G.T.L. was supported in part by a U.S. Department of Education GAANN fellowship. W.B.W. was supported by the Undergraduate Research Scholar Program of the NSF.

[‡] The atomic coordinates and structure factors have been deposited in the Protein Data Bank with the corresponding file names 2cdu and 2cdusf.

* To whom correspondence should be addressed. A.M.O.: e-mail, amorv@bnl.gov; phone, 631-344-4739; fax, 631-344-2741. A.S.B.: e-mail, andreas.bommarius@chbe.gatech.edu; phone, 404-385-1334; fax, 404-894-2291.

[§] School of Chemistry and Biochemistry and the Petit Institute for Bioengineering and Bioscience, Georgia Institute of Technology.

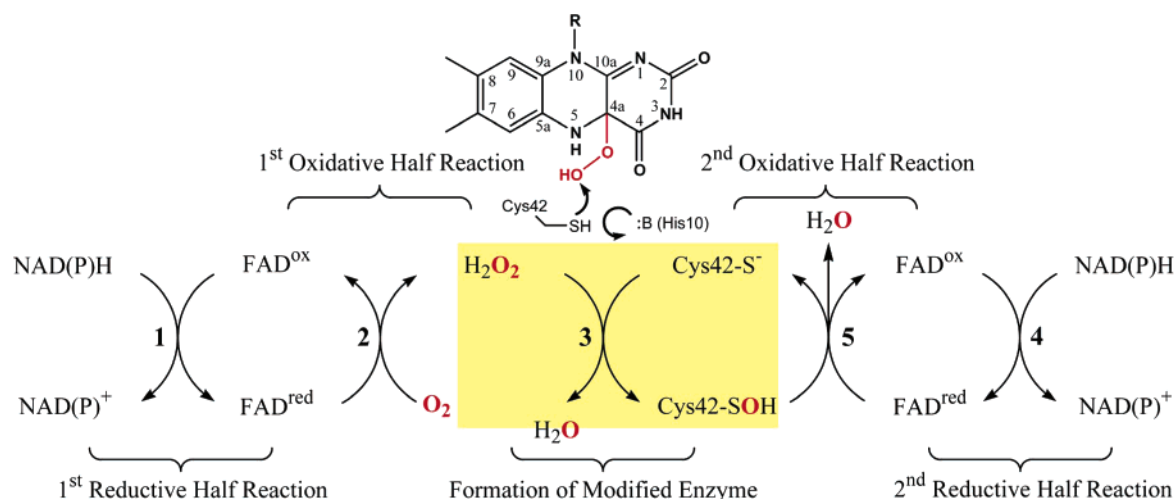
^{||} Current address: Macromolecular Crystallography Laboratory, Center for Cancer Research, National Cancer Institute at Frederick, Frederick, MD 21702-1201.

[⊥] School of Chemical and Biomolecular Engineering and the Petit Institute for Bioengineering and Bioscience, Georgia Institute of Technology.

^Δ Current address: School of Chemical and Biomedical Engineering, Nanyang Technological University, 16 Nanyang Drive, Singapore 637722.

[◇] Current address: Biocatalytics, Inc., 129 Hill Ave., Suite 103, Pasadena, CA 91106-1955.

[#] Current address: Biology Department, Brookhaven National Laboratory, Upton, NY 11973.

Scheme 1: Overall Reactions Catalyzed by NAD(P)H Oxidase^a

^a The FAD-C4a-OO(H) species generated in the active site does not release H₂O₂ and does not dissociate from the enzyme but rather reacts with the active site Cys42 (step 3 within the shaded box).

(Cys42 in *L.san*-Nox2) or the FAD and NAD(P)H binding domains. To our knowledge, no crystal structure has been reported for a H₂O-producing NAD(P)H oxidase, but sequence analysis suggests that these enzymes constitute a distinct class of FAD-dependent oxidoreductases. However, they are likely to be structurally related to the family of disulfide reductases (20), which include glutathione reductase (21), thioredoxin reductases (22), dihydrolipoamide dehydrogenases (23), trypanothione reductases (24), and LpDA from *Mycobacterium tuberculosis* (25).

A unique aspect of the *L.san*-Nox2 is that it oxidizes NADH and NADPH at a V_{\max} ratio of 3:1 but with very similar K_M values of 6.1 and 6.7 μ M, respectively. In contrast, the homologous enzyme from *L.lactis* (*L.lac*-Nox2) is specific for NADH (26). However, both *L.san*-Nox2 and *L.lac*-Nox2 do not release H₂O₂ during turnover but rather form two H₂O molecules from O₂ and 2 equiv of NAD(P)H (Scheme 1). Indeed, we have demonstrated that less than 0.5% of the reducing equivalents can be detected as H₂O₂ from either enzyme (26–28). Therefore, hydrogen peroxide must not be released from the enzyme during turnover. Two features of the reaction scheme warrant further comment. First, both the *L.san*-Nox2 and *L.lac*-Nox2 enzymes evolved mechanisms to facilitate the generation of H₂O₂, which is very common in flavoprotein oxidases (29, 30), but then to prevent it from escaping into the cytosol. This is particularly important for the facultative anaerobes that lack heme-based catalases to protect the organism from H₂O₂. Second, the *L.san*/*lac*-Nox2 also evolved a mechanism to enable O₂ reactivity at step 2, but not at step 5, as illustrated in Scheme 1. Indeed, aberrant H₂O₂ produced at step 5 would likely inactivate the enzyme via generation of a Cys-SOO(H)

intermediate and create additional oxidative stress to the organism.

Sequence analysis and correlation with related enzymes suggest that both *L.san*/*lac*-Nox2 enzymes use a redox-active cysteine residue (Cys42) that alternates between the thiol/thiolate and the sulfenic acid states during turnover (17, 31). Thus the first equivalents of NAD(P)H and O₂ do yield H₂O₂, which then reacts with Cys42 to form the Cys42-SOH intermediate and a water molecule. The second equivalent of NAD(P)H is then used to reduce the sulfenic acid intermediate to the thiolate and releases the second H₂O molecule. The role of the sulfenic acid intermediate is supported by analysis of Cys \rightarrow Ser mutants in homologous enzymes to create isoforms that produced H₂O₂ instead of water during turnover (31–33). Thus the *L.san*/*lac*-Nox2 and other homologues have evolved an efficient mechanism to protect the organism from oxidative stress. Moreover, the role of cysteine sulfenic acids in biology and oxidative stress is quite prevalent in nature including humans (34–38) and thus is currently garnering attention (32, 39). Oxidative stress is often caused by an imbalance of redox-active species in the cell, of which reactive oxygen species are the principle molecular propagators and include hydrogen peroxide, superoxide, hydroxyl radical, or even molecular O₂. Oxidative stress is implicated in the pathology of a wide range of human diseases such as atherosclerosis, hypertension, stroke, cancer, pathogenic infections, and neurodegenerative diseases such as Parkinson's disease (9, 38, 40–46).

Here we report the 1.8 Å resolution crystal structure of *L.san*-Nox2 and the MALDI-TOF analysis of ligands released from the enzyme. We compare the results with similar analytical studies and homology modeling of the *L.lac*-Nox2. The crystal structure of *L.san*-Nox2 confirms the presence of the active site cysteine sulfenic acid, which exhibits two alternate conformations. A tightly bound ADP ligand occupies each NAD(P)H binding domain, despite the fact that no exogenous ligand was added to the protein during the course of purification or crystallization. The entire ADP molecule fits the observed electron density well and suggests that NAD(P)H substrate ligands bind via an alternative access

¹ Abbreviations: *L.san*-Nox2, the NAD(P)H oxidase from *Lactobacillus sanfranciscensis*; *L.lac*-Nox2, the NADH oxidase from *Lactobacillus lactis*; *L.san*/*lac*-Nox2, both enzymes as referenced above; *E.fae*-Nox2, the NADH oxidase from *Enterococcus faecalis*; NPX, the NADH peroxidase from *E. faecalis*; hGR, human glutathione reductase; Cys-SOH or Cys42-SOH, sulfenic acid states of a cysteine residue or Cys42; Cys-SOO(H), the sulfinic acid state of a cysteine residue; MALDI-TOF, matrix-assisted laser desorption/ionization time-of-flight mass spectrometry; rms, root mean squared.

channel present in the *L.san*-Nox2 structure. In contrast, HPLC analytical results from the *L.lac*-Nox2 indicate that the homologue does not bind ADP. Therefore, we propose that *L.lac*-Nox2 binds NADH in the classic sense, and indeed several residues lining the NADH binding domain likely elicit the NADH specificity observed for the enzyme.

MATERIALS AND METHODS

Preparation, Crystallization, and Data Collection. The *L.san*-Nox2 was cloned, expressed, purified, and crystallized as previously reported (47). The *L.lac*-Nox2 was cloned, expressed, and purified as previously reported (26). X-ray diffraction data for *L.san*-Nox2 were collected from cryo-protected crystals held at approximately 100 K at beamline 22-ID of the SER-CAT facility of the Advanced Photon Source (APS), Argonne National Laboratory, and processed as previously reported (47). Briefly, the crystals crystallized in space group $P2_12_12_1$, diffracted up to 1.8 Å resolution, and contain two molecules per asymmetric unit. An additional data set was collected from another crystal of *L.san*-Nox2 grown in identical conditions in order to confirm the presence of a bound ADP in this structure as well. The crystal diffracted to a resolution of 2.1 Å with very similar unit cell dimensions. The structure description of *L.san*-Nox2 reported here will be based on the highest resolution (1.8 Å) structure.

Crystal Structure Determination. The structure of *L.san*-Nox2 was solved by molecular replacement using the NADH peroxidase [PDB code 1F8W (18)] as a search model and the program MOLREP (48, 49). The molecular replacement solution was initially subjected to rigid body refinement and simulated annealing with CNS (50) to a resolution of 3.0 Å. Manual model rebuilding was performed with the program O (51, 52), and the model was refined against the 1.8 Å resolution data using maximum likelihood refinement in the program REFMAC5 (49) from the CCP4 suite of programs (53). Progress of the refinement was monitored by R_{free} (54, 55), which was calculated using 5% of the reflections, and cross-validated, σ_A -weighted $2mF_o - DF_c$ and $mF_o - DF_c$ maps to evaluate the model and correct errors (56). Water molecules were located and refined in the final stages of refinement with ARP/Waters (57) and REFMAC5. The 2.1 Å resolution crystal structure was determined by subjecting the 1.8 Å structure to rigid body refinement against the 2.1 Å data followed by maximum likelihood refinement with REFMAC5. The ADP, FAD, and solvent molecules were removed from the model prior to the refinement, and the Cys42 residue was modeled as alanine to prevent model bias. The quality of the stereochemical parameters of the refined model was evaluated with PROCHECK (58, 59) and indicates good stereochemical properties.

The X-ray data collection and refinement statistics for *L.san*-Nox2 are shown in Table 1. The initial maps obtained after rigid body refinement and simulated annealing resulted in interpretable electron density with greater than 3σ positive difference features clearly visible for the active site FAD and the side chain atoms for many of the truncated residues. To minimize model bias, Cys42 was modeled as alanine until the majority of the structure was traced correctly into the maps. Each ADP molecule was fit into the greater than 6.5σ positive difference electron density features observed in the NADH binding domain in the latter stages of the model

Table 1: Data Collection and Model Refinement Statistics for *L.san*-Nox2

Data Collection	
space group	$P2_12_12_1$
unit cell dimensions (Å)	$a = 59.6, b = 92.6, c = 163.5$
resolution range (Å) ^a	46.4–1.8 (1.85–1.8)
total reflections	693981
unique reflections	81507
completeness (%)	96.1 (73.8)
multiplicity	8.5 (4.1)
$I/\sigma(I)$ ^b	29.0 (1.9)
R_{sym} (%) ^c	10.2 (48.9)
Model Refinement	
resolution range (Å)	46.4–1.8
no. of reflections	77370
R -factor	0.178
R_{free} ^d	0.223
no. of non-H protein atoms	6980
no. of FAD molecules	2
no. of ADP molecules	2
no. of water molecules	708
mean B	
protein atoms (Å ²)	27.1
FAD (Å ²)	22.7
ADP (Å ²)	48.0
water atoms (Å ²)	37.2
rms deviations from ideal	
bond lengths (Å)	0.015
bond angles (deg)	1.5
estimated coordinate error (Å)	0.136
correlation coefficient	0.965

^a Numbers in parentheses are for the highest resolution shell. ^b The average agreement between the independently measured intensities. ^c The root mean squared value of the intensity measurements divided by their estimated standard deviation. ^d Calculated with 5% of the data.

refinement. Simulated annealing OMIT maps were also calculated in CNS by omitting ADP, FAD, and Cys42 from the map calculations in order to check for model bias (50). The final model for *L.san*-Nox2 refined to an R -factor of 0.17 and R_{free} of 0.22 for data between 46.4 and 1.8 Å (77355 reflections). The 2.1 Å structure was refined to an R -factor of 0.20 and R_{free} of 0.26 for data between 50 and 2.1 Å (49877 reflections). Ramachandran analysis of the highest resolution structure showed that 90.3% of the residues were located in the most favored region, 9.3% in the additionally allowed region, 0.4% in generously allowed regions, and none in the disallowed region. The estimated overall coordinate error for the model based on the R -factor was 0.137 (0.132 for R_{free}), and the correlation coefficient of the maps was 0.965.

Solvent-exposed surface areas were calculated with a 1.4 Å probe radius with Swiss-PDB viewer (v3.7b2) (60) or VEGA (<http://www.ddl.unimi.it>) (61). Library files for the modified Cys42 residue and cofactors were made using the Dundee PRODRG server (62). Secondary structure assignments were made using KSDSSP (63). Structural homologues in the Protein Data Bank were found using MSDfold (64). The rms difference between models was calculated with the protein structure comparison service SSM at European Bioinformatics Institute (64) (<http://www.ebi.ac.uk/msd-serv/ssm>) or Swiss-PDB viewer (v3.7b2). Structure figures were prepared using Swiss-PDBViewer (v3.7b2) and PovRay (v3.5) or Pymol (DeLano Scientific LLC, Castro City, CA).

HPLC and Mass Spectrometry of Ligands. The supernatant containing released ligands from heat-denatured *L.san*-Nox2

was analyzed using MALDI-TOF mass spectrometry. Samples were prepared by gel filtration using a Sephadex G-25 column (PD-10) (Amersham-Pharmacia Biotech, Piscataway, NJ) and then heat denatured by boiling the enzyme for 1.5 h. MALDI-TOF spectra of the supernatant were collected using an ABI Voyager DE-pro mass spectrophotometer at the Georgia State University (Atlanta, GA) Mass Spectrometry Facility.

L.lac-Nox2 Purification and Analysis of Endogenous Ligand(s). The *L.lac-Nox2* was expressed with a C-terminal His tag and purified by using immobilized metal affinity chromatography as described previously (IMAC; BD Talon Co²⁺ Metal Affinity CellThru Resin; BD Biosciences, Palo Alto, CA) (65). The enzyme was then dialyzed overnight against 50 mM HEPES buffer, pH 7.0, using an ultrafiltration membrane with 12–14 kDa molecular mass cutoff (MWCO) (Spectrum Laboratories, Rancho Dominguez, CA) (26). The protein was denatured at 100 °C for 8 min and centrifuged at 12400g. The collected supernatant was analyzed by a Beckman Coulter System Gold 126 solvent module HPLC using a C₁₈ reversed-phase column (Beckman Coulter, 4.6 × 250 mm). A 5 min isocratic elution was run with 0.1 M ammonium acetate, pH 5.3, followed by a 25 min linear gradient to 50% methanol using a 1 mL/min flow rate. The eluted peaks were monitored by absorbance at 260 and 450 nm with a Beckman Coulter System Gold 168 detector. Authentic standards of 10 μM ADP (Sigma-Aldrich, St. Louis, MO) and 10 μM FAD (Sigma-Aldrich, St. Louis, MO) were also analyzed by these conditions. To one sample of the denatured protein supernatant was added 10 μM ADP and analyzed as above.

Homology Model of L.lac-Nox2. A homology model of *L.lac-Nox2* was generated using the crystal structure of *L.san-Nox2* as a template and the SWISS-MODEL automated comparative protein modeling server (<http://swiss-model.expasy.org/SWISS-MODEL.html>). The default “project (optimize) mode” was used for generation of the model (66). The FAD was added to the *L.lac-Nox2* model by superimposing the homology model onto the coordinates of the *L.san-Nox2* crystal structure and importing the coordinates of the FAD from *L.san-Nox2*.

RESULTS

Overall Structure Description of L.san-Nox2. The asymmetric unit contains one holoenzyme, which is composed of two identical subunits related by 2-fold symmetry (Figure 1A,B). Indeed, structural overlap between the two subunits yields a rms difference of approximately 0.4 Å. Each subunit is roughly divided into three major domains; an N-terminal FAD-binding domain (residues 1–120), a middle NAD(P)H binding domain (residues 150–250), and a C-terminal dimerization domain (residues 325–451). Approximately 6000 Å² is buried at the dimer interface, which corresponds to 30% of the surface area for each monomer. The C-terminal residue 452 in chain A and residues 450–452 in chain B were not visible in the electron density maps and were consequently not included in the model. The FAD and NAD(P)H binding domains both adopt a Rossman fold topology (Figure 1C), which are structurally very similar to each other (rms difference of 1.09 Å over 66 common C_α atoms). In addition to noncovalently bound FAD, the enzyme also

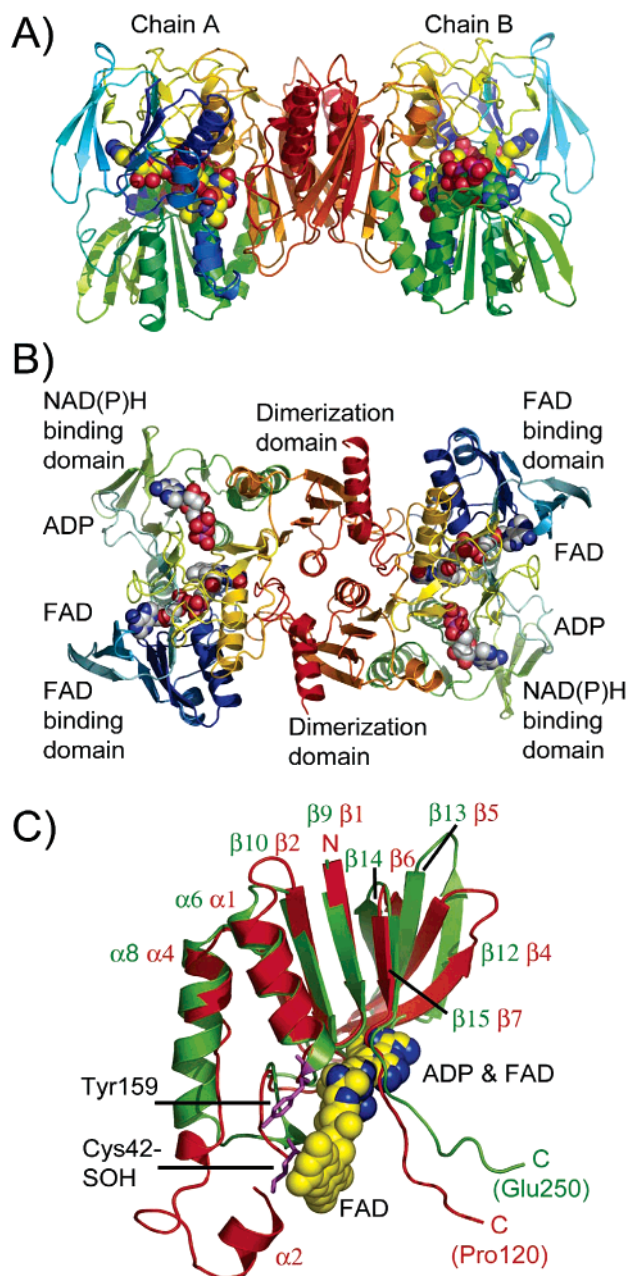


FIGURE 1: The crystal structure of *L.san-Nox2* illustrating (A) a view perpendicular to the 2-fold axis and (B) a view after an approximately 90° rotation about the horizontal axis. The FAD and ADP are shown as CPK atoms with the C, N, and O atoms colored in gray, blue, and red, respectively. (C) An overlay of the FAD domain (green, residues 1–120) and the NAD(P)H domain (red, residues 150–250) of *L.san-Nox2*. The FAD (yellow) and ADP (blue) are illustrated as CPK atoms. The Cys42-SOH and Tyr159 residues are shown in magenta sticks.

contains a bound ligand molecule in the NAD(P)H binding domain, which we have modeled as ADP (see below).

A High-Affinity Ligand in the NAD(P)H Domain. During the course of refinement, positive $mF_o - DF_c$ features at greater than 6.5σ persisted in the electron density maps in the NAD(P)H binding domain, suggesting the presence of a bound ligand. The electron density could be fit well with an adenine, ribose, and two phosphate moieties, but the electron density does not extend completely to the FAD *re*-face. Simulated annealing OMIT maps and the final refined models support the interpretation of ADP as the ligand

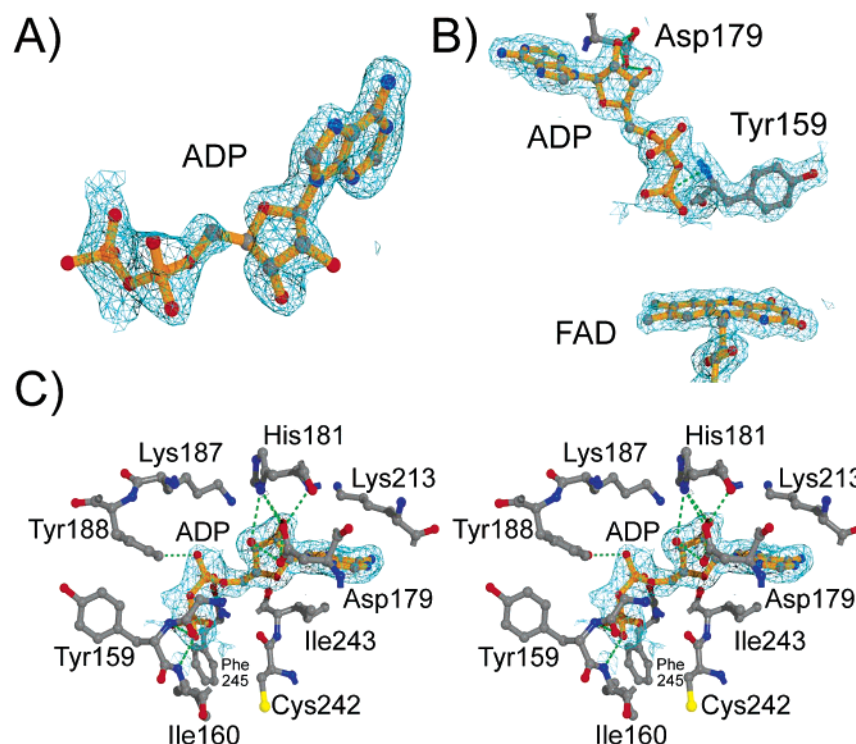


FIGURE 2: Typical electron density maps for the ADP ligand, FAD, and several residues. (A) The $2mF_o - DF_c$ simulated annealing OMIT electron density maps (contoured at 1σ , 1.8 Å resolution) obtained by omitting the ADP and FAD molecules from the map calculations superimposed with the final refined coordinates for the ADP ligand. (B) Relationship between the ADP and the FAD with the final $2mF_o - DF_c$ electron density maps (contoured at 1σ , 1.8 Å resolution). (C) A divergent stereoview of the ADP binding site in *L.san-Nox2*. The hydrogen-bonding interactions are represented by green dashed lines. The ADP molecule is superimposed upon the final $2mF_o - DF_c$ electron density maps (contoured at 1σ , 1.8 Å resolution). The bonds in the ADP molecule are colored in orange and the C, N, O, and S atoms of the amino acid residues are colored in gray, blue, red, and yellow, respectively.

(Figure 2). To confirm this assignment, the supernatant containing the ligands released from heat-denatured enzyme was analyzed by MALDI-TOF mass spectrometry (Supporting Information, Figure S1). The negative ion mode analysis reveals two sharp m/z ratios of 784 and 425.9 that correlate with the molecular weights of FAD and ADP, respectively. The ADP ligand occupies the NAD(P)H binding domain in an extended conformation with the diphosphate moiety toward the FAD *re*-face. There is no evidence for covalent attachment of the ligand to the enzyme. The side chain of Asp179 hydrogen bonds with the 2'-hydroxyl group of the ADP ribose ring. The two phosphate groups of the ADP are hydrogen bonded with the Ile160^N, Tyr159^N, and Tyr188^{OH} moieties. Additional hydrogen bonds are suggested between the ADP ribose hydroxyl groups and His181^{Ne2}. Approximately 11% of the total surface area for the ADP ligand is exposed to bulk solvent, which is consistent with high affinity. A second, independent crystal structure of *L.san-Nox2* to 2.1 Å resolution also reveals the presence of the tightly bound ADP ligand.

Comparisons of *L.san-Nox2* and *L.lac-Nox2*. Several remarkable similarities and differences become apparent when *L.san-Nox2* and *L.lac-Nox2* are compared. They share 33% amino acid sequence identity (Supporting Information, Table S1) including Cys42 and His10, which are essential features of the active site in *L.san-Nox2* (see below). The FAD to protein ratio can be estimated by the A_{260}/A_{450} ratios of each enzyme. Values of 10.2 and 7.89 for *L.san-Nox2* and *L.lac-Nox2* suggest that they each bind one FAD per subunit. However, *L.lac-Nox2* binds exogenously added FAD

with a K_M of 53 μM , whereas exogenously added FAD has no effect on *L.san-Nox2*. Importantly, *L.san-Nox2* oxidizes both NADH and NADPH with approximately equal affinity ($K_M = 6.7$ and 6.1 μM , respectively), whereas *L.lac-Nox2* will only oxidize NADH with a K_M of 90 μM . The maximal catalytic activities for each enzyme are as follows: *L.san-Nox2*, $k_{\text{cat}}(\text{NADH}) = 184 \text{ s}^{-1}$ and $k_{\text{cat}}(\text{NADPH}) = 52 \text{ s}^{-1}$, and *L.lac-Nox2*, $k_{\text{cat}}(\text{NADH}) = 78 \text{ s}^{-1}$. Thus *L.san-Nox2* has an apparent 3–4-fold preference for NADH over NADPH but nevertheless efficiently oxidizes both substrates. In contrast, *L.lac-Nox2* is specific for NADH. During steady-state turnover, both enzymes release between 0.4% and 0.7% of the stoichiometrically expected amount of hydrogen peroxide, suggesting mechanistic similarities that prevent H_2O_2 from dissociating from the enzymes. Our structures show that the putative NAD(P)H binding pocket in each *L.san-Nox2* subunit is occupied by an ADP molecule. Consequently, the A_{260}/A_{450} ratio of 9.27 and 6.3 for *L.san-Nox2* and *L.lac-Nox2*, respectively, is consistent with the presence of ADP in the former, but not in the latter. Indeed, HPLC analysis of the endogenous ligand(s) released from heat-denatured *L.lac-Nox2* indicates that only FAD binds to the enzyme as isolated (Supporting Information, Figure S2). Therefore, substrate preference in *L.lac-Nox2* is likely dictated by the residues lining the putative NADH binding domain (see below). In contrast, the presence of the ADP ligand in *L.san-Nox2* appears to be responsible, at least in part, for the lack of substrate preference by this homologue.

Active Site Architecture of *L.san-Nox2*. The electron density is unambiguous for the entire portion of the nonco-

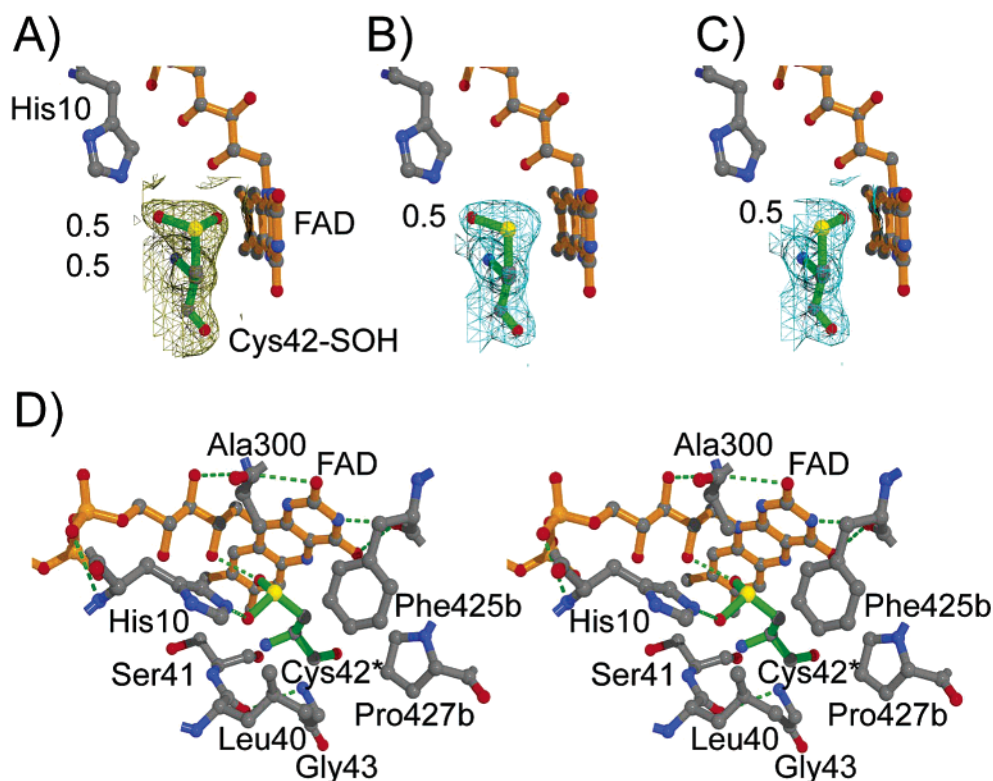


FIGURE 3: Structural analysis of the redox state of Cys42. (A) The $mF_o - DF_c$ positive difference electron density (gold, contoured at 3σ , 1.8 Å resolution) obtained from simulated annealing OMIT maps, with Cys42 omitted from the map calculations, superimposed upon the Cys42-SOH residue which is modeled with the distal oxygen occupying two alternate conformations with half-occupancy. (B, C) The Cys42-SOH residue exists in two alternate conformations and is stabilized by hydrogen-bonding interactions with either His10 or the FAD. Cys42-SOH also partially blocks access of O₂ to the FAD-C4a atom. The refined models in (B) and (C) are superimposed upon the final $2mF_o - DF_c$ electron density (blue, contoured at 1σ , 1.8 Å resolution). The bonds in the Cys42-SOH residue are colored in green and those of the FAD in orange. The C, N, O, and S atoms are colored in gray, blue, red, and yellow, respectively. (D) A divergent stereoview of the active site residues surrounding the *si*-face of the FAD and Cys42-SOH. The Cys42-SOH residue is colored in green and the C, N, O, and S atoms are colored as above.

valently bound FAD cofactor in each subunit. The electron density maps further indicate that the FAD isoalloxazine ring is bent slightly. The approximately 16° angle along the N5–N10 axis derives from the 168.4° angle between C6–N5–C4 atoms and the 169.6° angle between the C9–N10–N1 atoms. A portion of the FAD is shielded from the exterior solvent by the second subunit of the dimer (backbone of Pro424b, Phe235b, and Met236b). Indeed, within this contact region, the carbonyl oxygen of Phe423b hydrogen bonds with the FAD N3 and O4 atoms.

The electron density for the redox-active Cys42 residue located on the FAD *si*-face suggests that it is oxidized to the sulfenic acid (Cys42-SOH) and that it adopts two alternate conformations (Figure 3). The side chain in each conformation is stabilized by hydrogen bonding with either His10^{Nε2} or the O2' ribityl moiety of the FAD. Several refinement models were analyzed for this residue including Cys42-SH, Cys42-SO₂H, and Cys42-SO₃H. None of these models produced maps that were devoid of $mF_o - DF_c$ difference features and often the model had *B*-values for the S and/or O atoms that were very different than their adjacent bonded atoms. In contrast, a refinement model comprised of Cys42-SOH in two conformations, but each with 0.5 occupancy, produced maps with very well defined $2mF_o - DF_c$ electron density and no difference features. Moreover, the *B*-values for all atoms within the residue varied smoothly. In one orientation of Cys42-SOH the sulfenic acid moiety

hydrogen bonds with the imidazole of His10, and in the other it hydrogen bonds with the FAD and is only 3 Å from the C4a atom. Thus the latter orientation partially blocks access to the FAD C4a atom from the *si*-face. Additional models with occupancies for the two conformations that ranged in 10% increments from 1:0 to 0:1 were also analyzed, but these did not improve the models or maps. Two subtly different orientations of the His10 side chain (each with 0.5 occupancy) were observed to correlate with the fraction of Cys42-SOH that forms a hydrogen bond with it. Analysis of the protein environment around Cys42-SOH indicates that the residue is sequestered by mostly nonpolar residues (Leu40, Gly43 from chain A and Phe435, Pro427 from chain B).

DISCUSSION

Structural Homologues of *L.san*-Nox2. The structural analysis of *L.san*-Nox2 reveals structural homology with several members of the pyridine nucleotide disulfide reductase family of enzymes. Proteins with the highest degree of structural similarity are listed in Supporting Information, Table S2. These enzymes share very similar folds, despite sequence identities that range between 18% and 39%. (For a sequence alignment and secondary structure assignment for *L.san*-Nox2, please see Supporting Information, Figure S3.) The closest structural homologue is NADH peroxidase (NPX) from *E. faecalis* [PDB code 1JOA (16)], which

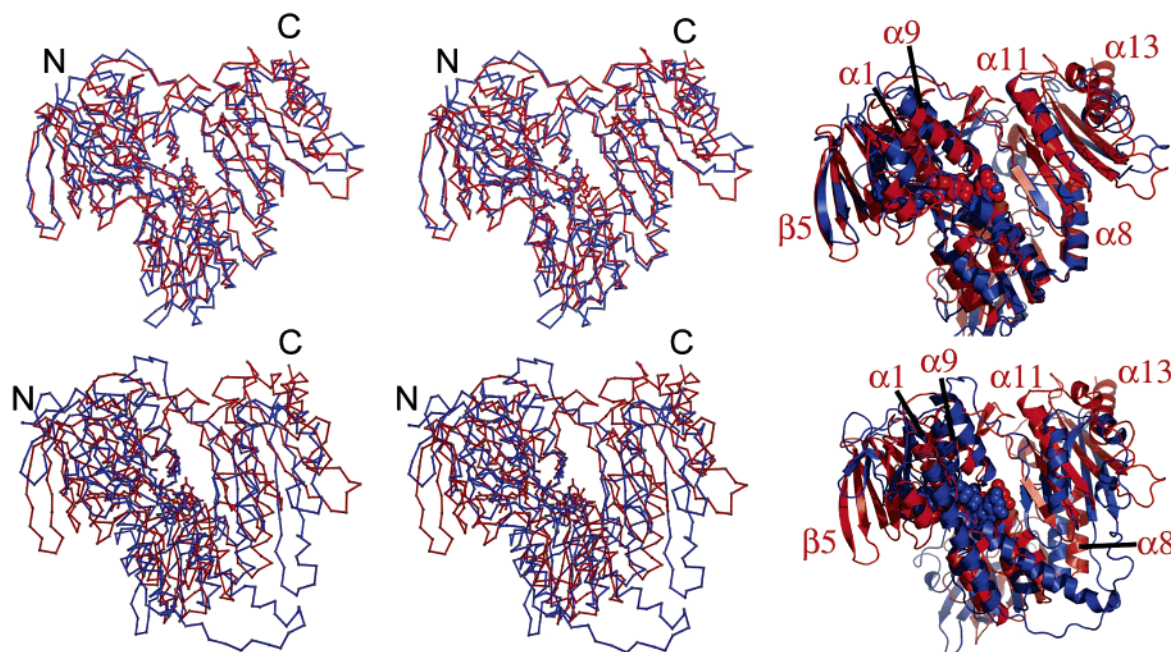


FIGURE 4: A divergent stereoview of the C_{α} trace of (top) *L.san-Nox2* (red) superimposed with NADH peroxidase (blue; PDB code 1joa) and (bottom) *L.san-Nox2* (red) superimposed with human glutathione reductase (blue; PDB code 1gra). The protein backbone ribbon trace for the superimposed enzymes is shown on the right with the FAD shown as space-filled atoms and colored as in the C_{α} traces. Selected structural elements are labeled.

exhibits rms deviations of 1.45 Å over 439 common C_{α} atoms when the monomers are superimposed (Figure 4).

The subunit structures of *L.san-Nox2* and human glutathione reductase (hGR) overlay with rms differences of approximately 2.8 Å over 329 common C_{α} atoms (Figure 4). The overall fold is very similar, and both proteins exhibit roughly the same topology of secondary structural elements and domains (21). Analysis of the molecular surface of the *L.san-Nox2* and hGR reveals that both share homology in the active site, which includes the redox-active cysteine residues. The *L.san-Nox2* Cys42 residue is analogous to the hGR Cys63 residue, and the nearby Cys58 residue in hGR allows for the formation of a redox-active disulfide bond (70). The structural overlays for the monomers of *L.san-Nox2* and hGR are more similar to each other than when the two dimeric proteins superimposed. Analysis of the two dimeric structures reveals that although the molecules in one subunit superimpose well, the second subunits do not (rms difference of 34.8 Å for residues 18–450). Thus, there is a significant shift in the orientation of the second subunit in hGR when compared to the analogous subunit in *L.san-Nox2*.

Comparison of *L.san-Nox2* with NADH Peroxidase. The monomers of *L.san-Nox2* and NADH peroxidase superimpose with an rms difference of 1.4 Å over 439 common C_{α} atoms (Figure 4, Supporting Information, Table S2). However, when the *L.san-Nox2* dimer is superimposed with the analogous NADH peroxidase dimer, the rms difference increases to approximately 1.9 Å (for 956 common C_{α} atoms). Some of the largest structural deviations are found in the FAD binding domain (residues 1–119). For example, superposition of 119 C_{α} atoms comprising an individual FAD domain from each enzyme yields an overlay with rms deviation of ~4.8 Å. However, the value increases to ~6.2 Å when the overlay is calculated with both FAD domains from the dimer of each protein. In comparison, the overlays of the NAD(P)H binding domains (approximately residues

150–250) increase by only 0.5 Å rms difference for overlays of respective monomer or dimer structures. Consequently, the two enzymes have slightly different orientations of the secondary structure elements in the FAD binding domains with respect to the NAD(P)H domains. Despite these similarities and differences, the most striking difference between the two enzymes is the presence of an ADP molecule in the NAD(P)H binding domain of *L.san-Nox2*. Indeed, the ligand is clearly present even though it was never added during expression, purification, or crystallization of the enzyme. In contrast, the structure of NADH peroxidase as isolated does not contain a bound ligand within the NADH binding domain.

A comparison of the active site environment between NADH peroxidase (with at least sulfenic acid present at Cys42) and *L.san-Nox2* reveals further similarities and differences (Figure 5A). For example, His10 and Cys42 are conserved among the two structures, but the relative positions of the C_{α} atom for His10 and Cys42 differ by 1.2 and 0.7 Å, respectively. Furthermore, the side chain of His10 in *L.san-Nox2* is observed in two alternate conformations, each with half-occupancy. The hydrogen-bonding environment also differs for these two residues. In the NADH peroxidase structure, the proximal oxygen of Cys42-SOH hydrogen bonds with the FAD N5 atom (3.2 Å) and is within 3.4 Å of the His10^{Ne2} atom. In contrast, in the *L.san-Nox2* structure the side chain of Cys42-SOH hydrogen bonds with either the FAD O2' atom (2.5 Å) or the His10^{Ne2} atom (3.2 Å) depending on the conformation of Cys42-SOH. Additional differences exist among residues lining the solvent access channel to the *si*-face of the FAD. In NADH peroxidase, an ionic interaction between Glu14 and Arg303 is present, and furthermore, the Arg303^{N1} atom hydrogen bonds with His10^{Ne1}. These ionic interactions are absent in *L.san-Nox2* because the analogous residues are nonpolar (Phe14 and Val304, respectively).

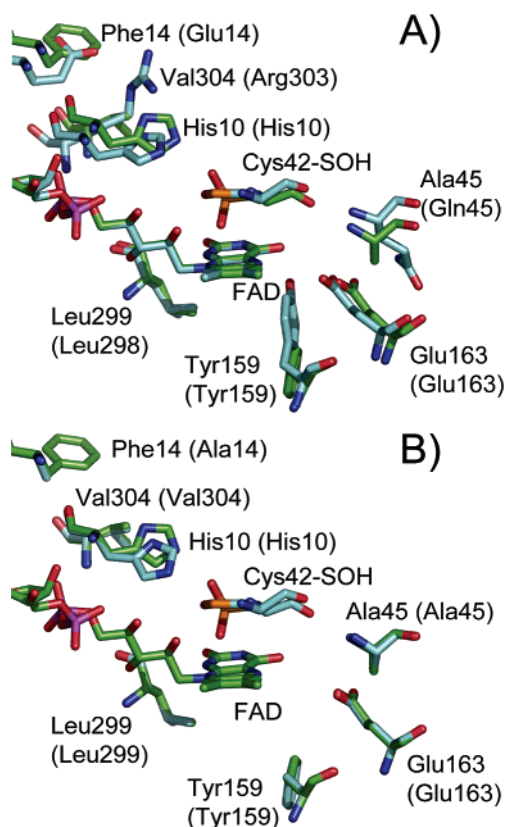


FIGURE 5: Active site structural comparisons of *L.san-Nox2* with NADH peroxidase and the hypothetical model of *L.lac-Nox2*. (A) The carbon atoms of *L.san-Nox2* are colored in green and those of NADH peroxidase are cyan (PDB code 1joa). The labels in parentheses correspond to the NADH peroxidase residues. (B) The color scheme for *L.san-Nox2* is as in (A), whereas the *L.lac-Nox2* carbon atoms are in cyan. The residue labels in parentheses correspond to the *L.lac-Nox2*. In both parts, the N, O, S, and P atoms are colored in blue, red, yellow, and magenta, respectively.

Comparison of *L.san-Nox2* and the Homology Model of *L.lac-Nox2*. The homology model of *L.lac-Nox2* was based upon the 33% sequence identity between the two enzymes and threaded onto our crystal structure of *L.san-Nox2*. The homology extends throughout the subunit of *L.san-Nox2* and includes the dimerization domain, which is consistent with a dimer structure for *L.lac-Nox2*. Moreover, the homology model of *L.lac-Nox2* suggests that it and *L.san-Nox2* share very similar active sites (Figure 5B). For example, His10, Cys42, Ala45, Tyr159, Val304, and Leu299 are all structurally conserved. Thus the solvent channel leading to Cys42 in *L.lac-Nox2* includes nonpolar residues more similar to *L.san-Nox2* and in contrast to the Glu14 and Arg303 residues in the NADH peroxidase. Other significant differences between the *L.san-Nox2* and *L.lac-Nox2* include the environment comprising the NAD(P)H binding domain (see below).

NAD(P)H Substrate Binding. Prior results from our laboratories have shown that *L.san-Nox2* exhibits dual substrate specificity (27, 28). Indeed, both NADH and NADPH have almost identical K_M values (6.7 and 6.1 μM , respectively). The crystal structure of *L.san-Nox2* reveals three channels that extend from the surface of the protein to the active site. One channel terminates at the FAD *re*-face, the second terminates at the Cys42 and the FAD *si*-face, and the third extends along the subunit interface and terminates

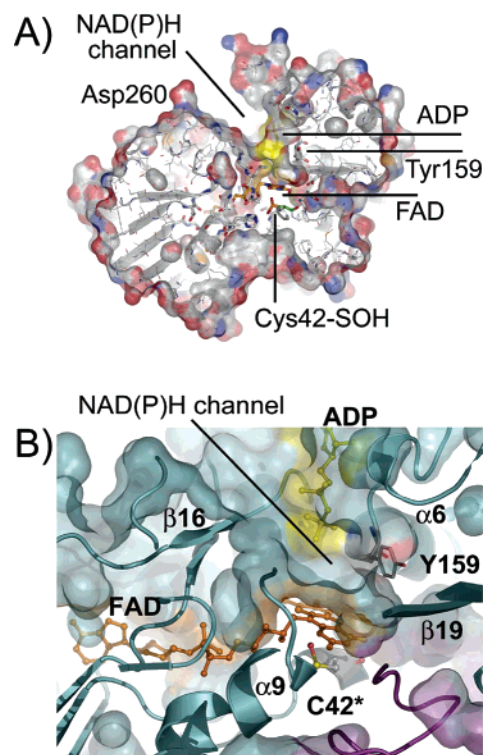


FIGURE 6: The solvent-excluded surface area of *L.san-Nox2*. (A) The putative entrance channel for NAD(P)H that terminates at the *re*-face of the FAD. The surfaces associated with the bound ADP are displayed in yellow, whereas the protein surfaces are colored according to atom type, with C, N, and O as white, blue, and red, respectively. (B) The active site cavity at the FAD *re*-face can accommodate the nicotinamide ring of a bound NAD(P)H molecule. The surface area of the ADP ligand within the NAD(P)H domain is colored yellow, the surfaces associated with the FAD are in orange, and the surfaces associated with the protein subunits are in either cyan or purple. There is a channel connecting the *re*- and *si*-faces of the FAD and terminates at Cys42 that is of sufficient size to permit migration of H₂O₂.

at the C4a edge of the FAD isoalloxazine ring (Figure 6). The channel terminating at the FAD *si*-face in *L.san-Nox2* is lined primarily with hydrophobic residues. In NADH peroxidase, the homologous channel is lined with more polar residues and is proposed to be the channel in which H₂O₂ is delivered to the active site (18). The *si*-face channel is also approximately analogous to the glutathione binding region in hGR. The channel terminating at the *re*-face in *L.san-Nox2* is lined by residues Ser115, Phe245, Asp282, Tyr296, Pro298, and Leu299 and by the ribose ring and phosphate moieties of the ADP ligand.

Dual substrate specificity observed in *L.san-Nox2* can be rationalized in at least two ways (discussed here and below). One hypothesis assumes that the ADP ligand remains bound to the enzyme during turnover. Consequently, the NAD(P)H substrates may access the FAD via the large *re*-face channel observed in the structure. The nicotinamide ring from either NADH or NADPH can be appropriately positioned adjacent to the isoalloxazine ring, provided that Tyr159 is rotated out of the way (see below). In contrast, NADH specificity in the other homologues is due, in part, to the amino acid residue located 19–21 residues downstream of the last glycine in the GXGXXG signature motif (34, 67–69). In general, NADP⁺ specificity derives from an arginine at this position, which provides ionic and hydrogen-bonding inter-

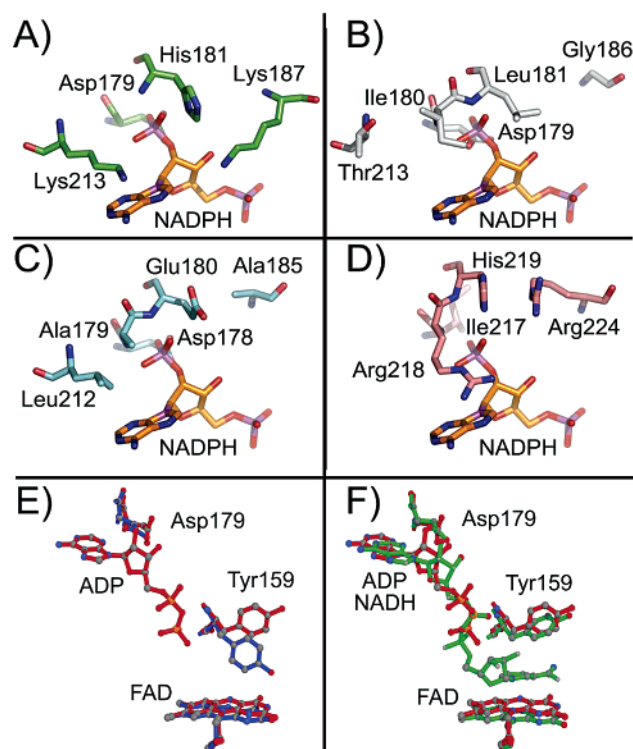


FIGURE 7: Structural comparisons of the NADPH binding domains in selected homologues. Note that the environment around the 2'-phosphate group in NADPH suggests a structural basis for substrate preference in each enzyme. (A) The *L. san*-Nox2 with NADP⁺ docked (protein carbon atoms in green, NADP⁺ carbon atoms in orange) into the binding site by superimposing *L. san*-Nox2 with the structure of the NADP⁺ complex of human glutathione reductase (PDB code 1gra). (B) The NADH peroxidase with carbon atoms in gray from the PDB (2npx). (C) The hypothetical model of *L. lac*-Nox2 with NADP⁺ docked by the same process described above. (D) The NADP⁺ complex of human glutathione reductase with carbon atoms in magenta from the PDB (1gra). (E) Structural overlays of the ADP bound in *L. san*-Nox2 and two forms of NADH peroxidase. The superimposed structures of *L. san*-Nox2 (red) and unliganded NADH peroxidase (blue; PDB code 1joa). (F) The superimposed structures of *L. san*-Nox2 (red) and NADH peroxidase in complex with NADH (green; PDB code 2npx). The conformation of Tyr159 in *L. san*-Nox2 is similar to that observed in the NADH complex of NADH peroxidase.

actions with the 2'-phosphate of NADP⁺. In contrast, NAD⁺ specificity derives from an acidic amino acid at this position, which hydrogen bonds with the 2'-hydroxyl group and provides for electrostatic selection against NADPH ligands. In *L. san*-Nox2, Asp179 occupies this important position and hydrogen bonds with the 2'-hydroxyl group of the ADP molecule (Figure 7). In *L. lac*-Nox2 and in *E. fac*-Nox2, the residue is conserved as Asp178. However, our HPLC analysis of denatured *L. lac*-Nox2 indicates that it does not contain a high-affinity ADP ligand. Consequently, we can rationalize specificity toward NADH and exclusion of NADPH in the *L. lac*-Nox2 as dictated by residues lining the putative NADH binding site. In contrast, the occupancy of ADP in the *L. san*-Nox2 typical NADH domain requires that NAD(P)H substrates must access the FAD via the larger channel, which lacks the typical interactions to dictate strict substrate preference.

To gain further structural insights for the different substrate preferences exhibited by the homologues, we docked NADPH into the NADH binding domains of the crystal structures

of *L. san*-Nox2, NADH peroxidase, and the homology model of *L. lac*-Nox2 (Figure 7). The conformation of the NADPH ligand was duplicated from the crystal structure of the NADPH complex of human glutathione reductase. The homology model of *L. lac*-Nox2 suggests that Asp178 would interact with the 2'-hydroxyl/phosphate group of the NAD(P)H substrate. Moreover, there are no residues within the vicinity of the 2'-phosphate that would stabilize the negative charge of the NADPH molecule. Consequently, *L. lac*-Nox2 should be specific for NADH, as observed with in vitro assays.

The second hypothesis for dual substrate specificity in *L. san*-Nox2 assumes that the ADP ligand departs during turnover, and that NAD(P)H subsequently binds in an analogous position as the observed ADP ligand. The residues lining the *L. san*-Nox2 putative NADH binding site suggest that the enzyme may accommodate either NADH or NADPH. For example, NADH or NADPH binding could be essentially analogous to the ADP ligand observed in the current structure. We do not forecast any significant alterations to protein side chains to accommodate NADH binding, with the exception of Tyr159, which is also applicable to the NADPH binding modes as well (see below). However, a slight conformational change of Asp179, which is possible on the basis of examination of alternative rotomers, would be required to move the negative charge of the side chain away from the region nearest the 2'-phosphate group of a bound NADPH substrate. In further support of this binding mode, we note that Lys213, His181, and Lys187 are all positioned to either hydrogen bond and/or stabilize the charge of such a bound NADPH molecule. Indeed, these interactions are analogous to those in NADPH complex of glutathione reductase (70). In contrast and as noted above, there are no positively charged residues within the vicinity of the 2'-phosphate group of the docked NADPH in either the model for *L. lac*-Nox2 or the NADH peroxidase structure. Consequently, the structures predict that these latter enzymes should not oxidize NADPH.

Orientation of Tyr159. An examination of the sequence alignments of *L. san*-Nox2, *L. lac*-Nox2, NADH peroxidase, and hGR reveals that Tyr159 in *L. san*-Nox2 is highly conserved. Moreover, the structural comparisons discussed above for the *L. san*-Nox2, NPX-NADH, and hGR-NADP⁺ complexes indicate that the ADP molecule in *L. san*-Nox2 occupies an analogous position as the adenosine dinucleotide portion of NADH in the other two structures (70, 72). However, the various crystal structures from these homologues obtained with and without ligands bound indicate that the equivalent Tyr159 residues occupy one of two orientations (Figure 7E,F). In the absence of ligands, the tyrosine conformation is typically in the "in" orientation, where it partially occludes the FAD *re*-face and especially at C4a. In contrast, when Tyr159 is in the "out" conformation, it likely permits ligand binding and hydride transfer to the FAD. Thus the crystal structures of the NADH complex of NADH peroxidase, the hGR-NADP⁺ complex, and the *L. san*-Nox2 structure reported here indicate that Tyr159 occupies the out position (70, 72). The orientation of the Tyr159^{OH} in *L. san*-Nox2 is influenced by a hydrogen bond with Ser328^{OH}, which stabilizes the out rotomer. However, a conformational change at Tyr159 would easily yield the in rotomer and would presumably decrease NAD(P)H and/or O₂ affinity. Therefore,

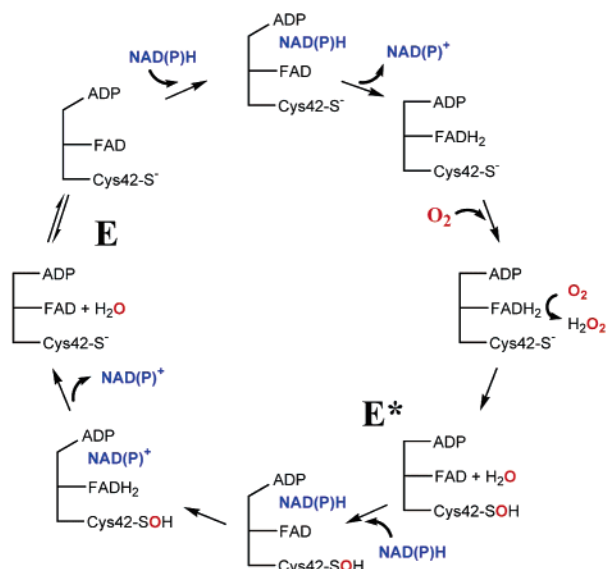


FIGURE 8: Proposed reaction cycle for *L. san-Nox2*.

Tyr159 may serve as a gate or sensor that modulates reactivity at the FAD C4a position.

Mechanistic Insights. The high-resolution crystal structure of *L. san-Nox2* and the homology model of *L. lac-Nox2* provide insights into the reaction mechanism for each enzyme (Figure 8). The oxidation state of the redox-active Cys42 residue is proposed to alternate between the thiol/thiolate (E) and the sulfenic acid states (E*) during turnover (32). Thus the observation of Cys42-SOH in *L. san-Nox2* provides critical information for rationalizing the observation that very little H₂O₂ is released from the active site of *L. san-Nox2* during turnover. Because a C4a-peroxy intermediate has been observed in the *E. faecalis* NADH oxidase C42S mutant (33), we assume that molecular oxygen reacts at the FAD C4a position and likely forms a peroxy flavin adduct. However, our structural analysis does not unambiguously suggest either a *re*- or *si*-face FAD peroxy adduct. We propose that the first equivalent of NAD(P)H used in the first oxidative half-reaction enters the active site via a *re*-face channel. Hydride transfer then yields reduced FAD and NAD(P)⁺, which may or may not dissociate readily. Subsequent reaction with O₂ yields H₂O₂, but it does not dissociate from the enzyme via the *re*-face because the channel is blocked by either (a) the NAD(P)⁺ product, (b) the ADP ligand, or (c) the in rotamer of Tyr159. Together, these factors serve to influence H₂O₂ migration toward the *si*-face by steric occlusion, where it encounters the thiolate moiety of Cys42. Nucleophilic attack of Cys42-S[−] on H₂O₂ will yield the first water molecule and generate the Cys42-SOH intermediate (E*), which is stabilized via hydrogen bonds to His10 and the FAD. Indeed, our crystal structure is most consistent with the E* form indicated in the reaction mechanism. The second equivalent of NAD(P)H then reduces the FAD. However, since the reduced FAD is in van der Waals contact with Cys42-SOH, it transfers two electrons to Cys42-SOH much faster than another reaction with O₂ to yield a second equivalent of H₂O₂. Thus the sulfenic acid is converted back to the thiolate, and the second H₂O molecule is released. The importance of Cys42 has been demonstrated by site-directed mutagenesis in NADH peroxidase in which Cys42 was mutated to Ala or Ser and also in the C42S mutant of *E. faecalis* NADH

oxidase. The two NPX mutants failed to react with H₂O₂, and the C42S mutant of the NADH oxidase generated H₂O₂ rather than H₂O (31, 33, 73).

Conclusion. To our knowledge, the high-resolution crystal structure of *L. san-Nox2* is the first structure of a water-forming, FAD-dependent NADH oxidase. The X-ray structure confirms that *L. san-Nox2* is a structural homologue of the pyridine nucleotide disulfide reductase family of enzymes and most closely resembles the structure of NADH peroxidase. The structure reveals that Cys42 is appropriately positioned to react with H₂O₂ to yield the first H₂O molecule and Cys42-SOH, which can then be reduced by the second equivalent of NAD(P)H. Furthermore, the discovery of a high-affinity ADP molecule, which copurifies and cocrystallizes with the enzyme, suggests a structural basis for the lack of substrate preference in *L. san-Nox2*. Our comparison of the *L. san-Nox2* and the hypothetical model of the *L. lac-Nox2* supports the hypothesis that the presence or absence of a bound ADP ligand influences substrate preference in the two enzymes. The structure of *L. san-Nox2* will also provide critical information in its development as a biocatalyst for the regeneration of oxidized pyridine nucleotides (27, 28).

ACKNOWLEDGMENT

Portions of this work were carried out at beamline 22-ID in the SER-CAT facilities at the Advanced Photon Source (APS). The use of APS is supported by the U.S. Department of Energy, Basic Sciences, Office of Science, under Contract W-31-109-Eng-38. We thank the staff at beamline 22-ID of the SER-CAT facilities at APS for assistance during data collection and Dr. Zhongmin Jin for assistance with the mail-in crystallography program at SER-CAT. We thank Dr. Kris Woods, Tatsuya Maehigashi, and Derrick Watkins for assistance with data collection. We also thank Prof. G. Gadda and Mr. M. Ghanem for assistance with the mass spectral analysis of *L. san-Nox2* ligands.

SUPPORTING INFORMATION AVAILABLE

Three figures and two tables as described in the text. This material is available free of charge via the Internet at <http://pubs.acs.org>.

REFERENCES

- Gobbetti, M., and Corsetti, A. (1997) *Lactobacillus sanfrancisco* a key sourdough lactic acid bacterium: a review, *Food Microbiol.* 14, 175–188.
- Bolotin, A., Wincker, P., Mauger, S., Jaillon, O., Malarme, K., Weissenbach, J., Ehrlich, S. D., and Sorokin, A. (2001) The complete genome sequence of the lactic acid bacterium *Lactococcus lactis* ssp. *lactis* IL1403, *Genome Res.* 11, 731–753.
- Kleerebezem, M., Boekhorst, J., van Kranenburg, R., Molenaar, D., Kuipers, O. P., Leer, R., Turchini, R., Peters, S. A., Sandbrink, H. M., Fiers, M. W., Stiekema, W., Lankhorst, R. M., Bron, P. A., Hoffer, S. M., Groot, M. N., Kerkhoven, R., de Vries, M., Ursing, B., de Vos, W. M., and Siezen, R. J. (2003) Complete genome sequence of *Lactobacillus plantarum* WCFS1, *Proc. Natl. Acad. Sci. U.S.A.* 100, 1990–1995.
- Siezen, R. J., van Enckevort, F. H., Kleerebezem, M., and Teusink, B. (2004) Genome data mining of lactic acid bacteria: the impact of bioinformatics, *Curr. Opin. Biotechnol.* 15, 105–115.
- de Vos, W. M., Bron, P. A., and Kleerebezem, M. (2004) Post-genomics of lactic acid bacteria and other food-grade bacteria to discover gut functionality, *Curr. Opin. Biotechnol.* 15, 86–93.

6. Klaenhammer, T., Altermann, E., Arigoni, F., Bolotin, A., Breidt, F., Broadbent, J., Cano, R., Chaillou, S., Deutscher, J., Gasson, M., van de Guchte, M., Guzzo, J., Hartke, A., Hawkins, T., Hols, P., Hutkins, R., Kleerebezem, M., Kok, J., Kuipers, O., Lubbers, M., Maguin, E., McKay, L., Mills, D., Nauta, A., Overbeek, R., Pel, H., Pridmore, D., Saier, M., van Sinderen, D., Sorokin, A., Steele, J., O'Sullivan, D., de Vos, W., Weimer, B., Zagorec, M., and Siezen, R. (2002) Discovering lactic acid bacteria by genomics, *Antonie Van Leeuwenhoek* 82, 29–58.
7. De Angelis, M., and Gobbetti, M. (2004) Environmental stress responses in *Lactobacillus*: a review, *Proteomics* 4, 106–122.
8. Poole, L. B. (2005) Bacterial defenses against oxidants: mechanistic features of cysteine-based peroxidases and their flavoprotein reductases, *Arch. Biochem. Biophys.* 433, 240–254.
9. Baker, L. M., Raudonikienė, A., Hoffman, P. S., and Poole, L. B. (2001) Essential thioredoxin-dependent peroxiredoxin system from *Helicobacter pylori*: genetic and kinetic characterization, *J. Bacteriol.* 183, 1961–1973.
10. Klenk, H. P., Clayton, R. A., Tomb, J. F., White, O., Nelson, K. E., Ketchum, K. A., Dodson, R. J., Gwinn, M., Hickey, E. K., Peterson, J. D., Richardson, D. L., Kerlavage, A. R., Graham, D. E., Kyrpides, N. C., Fleischmann, R. D., Quackenbush, J., Lee, N. H., Sutton, G. G., Gill, S., Kirkness, E. F., Dougherty, B. A., McKenney, K., Adams, M. D., Loftus, B., Venter, J. C., et al. (1997) The complete genome sequence of the hyperthermophilic, sulphate-reducing archaeon *Archaeoglobus fulgidus*, *Nature* 390, 364–370.
11. De Angelis, M., Bini, L., Pallini, V., Cocconcelli, P. S., and Gobbetti, M. (2001) The acid-stress response in *Lactobacillus sanfranciscensis* CB1, *Microbiology* 147, 1863–1873.
12. Rabus, R., Ruepp, A., Frickey, T., Rattei, T., Fartmann, B., Stark, M., Bauer, M., Zibat, A., Lombardot, T., Becker, I., Amann, J., Gellner, K., Teeling, H., Leuschner, W. D., Glockner, F. O., Lupas, A. N., Amann, R., and Klenk, H. P. (2004) The genome of *Desulfotalea psychrophila*, a sulfate-reducing bacterium from permanently cold Arctic sediments, *Environ. Microbiol.* 6, 887–902.
13. Marty-Teyssset, C., de la Torre, F., and Garel, J. (2000) Increased production of hydrogen peroxide by *Lactobacillus delbrueckii* subsp. bulgaricus upon aeration: involvement of an NADH oxidase in oxidative stress, *Appl. Environ. Microbiol.* 66, 262–267.
14. Higuchi, M., Yamamoto, Y., Poole, L. B., Shimada, M., Sato, Y., Takahashi, N., and Kamio, Y. (1999) Functions of two types of NADH oxidases in energy metabolism and oxidative stress of *Streptococcus mutans*, *J. Bacteriol.* 181, 5940–5947.
15. Gibson, C. M., Mallett, T. C., Claiborne, A., and Caparon, M. G. (2000) Contribution of NADH oxidase to aerobic metabolism of *Streptococcus pyogenes*, *J. Bacteriol.* 182, 448–455.
16. Yeh, J. I., Claiborne, A., and Hol, W. G. (1996) Structure of the native cysteine-sulfenic acid redox center of enterococcal NADH peroxidase refined at 2.8 Å resolution, *Biochemistry* 35, 9951–9957.
17. Crane, E. J., III, Yeh, J. I., Luba, J., and Claiborne, A. (2000) Analysis of the kinetic and redox properties of the NADH peroxidase R303M mutant: correlation with the crystal structure, *Biochemistry* 39, 10353–10364.
18. Stehle, T., Ahmed, S. A., Claiborne, A., and Schulz, G. E. (1991) Structure of NADH peroxidase from *Streptococcus faecalis* 10C1 refined at 2.16 Å resolution, *J. Mol. Biol.* 221, 1325–1344.
19. Beres, S. B., Sylva, G. L., Barbican, K. D., Lei, B., Hoff, J. S., Mammarella, N. D., Liu, M. Y., Smoot, J. C., Porcella, S. F., Parkins, L. D., Campbell, D. S., Smith, T. M., McCormick, J. K., Leung, D. Y., Schlievert, P. M., and Musser, J. M. (2002) Genome sequence of a serotype M3 strain of group A *Streptococcus*: phage-encoded toxins, the high-virulence phenotype, and clone emergence, *Proc. Natl. Acad. Sci. U.S.A.* 99, 10078–10083.
20. Kuriyan, J., Krishna, T. S., Wong, L., Guenther, B., Pahler, A., Williams, C. H., Jr., and Model, P. (1991) Convergent evolution of similar function in two structurally divergent enzymes, *Nature* 352, 172–174.
21. Karplus, P. A., and Schulz, G. E. (1987) Refined structure of glutathione reductase at 1.54 Å resolution, *J. Mol. Biol.* 195, 701–729.
22. Waksman, G., Krishna, T. S., Williams, C. H., Jr., and Kuriyan, J. (1994) Crystal structure of *Escherichia coli* thioredoxin reductase refined at 2 Å resolution. Implications for a large conformational change during catalysis, *J. Mol. Biol.* 236, 800–816.
23. Mattevi, A., Obmolova, G., Kalk, K. H., van Berkel, W. J., and Hol, W. G. (1993) Three-dimensional structure of lipoamide dehydrogenase from *Pseudomonas fluorescens* at 2.8 Å resolution. Analysis of redox and thermostability properties, *J. Mol. Biol.* 230, 1200–1215.
24. Zhang, Y., Bond, C. S., Bailey, S., Cunningham, M. L., Fairlamb, A. H., and Hunter, W. N. (1996) The crystal structure of trypanothione reductase from the human pathogen *Trypanosoma cruzi* at 2.3 Å resolution, *Protein Sci.* 5, 52–61.
25. Argyrou, A., Vetting, M. W., and Blanchard, J. S. (2004) Characterization of a new member of the flavoprotein disulfide reductase family of enzymes from *Mycobacterium tuberculosis*, *J. Biol. Chem.* 279, 52694–52702.
26. Jiang, R., Riebel, B. R., and Bommarius, A. S. (2005) Comparison of alkyl hydroperoxide reductase (AhpR) and water-forming oxidase from *Lactococcus lactis* ATCC 19435, *Adv. Synth. Catal.* 347, 1139–1146.
27. Riebel, B. R., Gibbs, P. R., Wellborne, W. B., and Bommarius, A. S. (2002) Cofactor regeneration of NAD⁺ from NADH: Novel water-forming NADH oxidases, *Adv. Synth. Catal.* 344, 1156–1168.
28. Riebel, B. R., Gibbs, P. R., Wellborne, W. B., and Bommarius, A. S. (2003) Cofactor regeneration of both NAD⁺ from NADH and NADP⁺ from NADPH:NADH oxidase from *Lactobacillus sanfranciscensis*, *Adv. Synth. Catal.* 345, 707–712.
29. Fraaije, M. W., and Mattevi, A. (2000) Flavoenzymes: diverse catalysts with recurrent features, *Trends Biochem. Sci.* 25, 126–132.
30. Massey, V. (2000) The chemical and biological versatility of riboflavin, *Biochem. Soc. Trans.* 28, 283–296.
31. Mande, S. S., Parsonage, D., Claiborne, A., and Hol, W. G. (1995) Crystallographic analyses of NADH peroxidase Cys42Ala and Cys42Ser mutants: active site structures, mechanistic implications, and an unusual environment of Arg303, *Biochemistry* 34, 6985–6992.
32. Claiborne, A., Yeh, J. I., Mallett, T. C., Luba, J., Crane, E. J., III, Charrier, V., and Parsonage, D. (1999) Protein-sulfenic acids: diverse roles for an unlikely player in enzyme catalysis and redox regulation, *Biochemistry* 38, 15407–15416.
33. Mallett, T. C., and Claiborne, A. (1998) Oxygen reactivity of an NADH oxidase C42S mutant: evidence for a C(4a)-peroxyflavin intermediate and a rate-limiting conformational change, *Biochemistry* 37, 8790–8802.
34. Duax, W. L., Pletnev, V., Addlagatta, A., Bruenn, J., and Weeks, C. M. (2003) Rational proteomics. I. Fingerprint identification and cofactor specificity in the short-chain oxidoreductase (SCOR) enzyme family, *Proteins* 53, 931–943.
35. Canet-Aviles, R. M., Wilson, M. A., Miller, D. W., Ahmad, R., McLendon, C., Bandyopadhyay, S., Baptista, M. J., Ringe, D., Petsko, G. A., and Cookson, M. R. (2004) The Parkinson's disease protein DJ-1 is neuroprotective due to cysteine-sulfenic acid-driven mitochondrial localization, *Proc. Natl. Acad. Sci. U.S.A.* 101, 9103–9108.
36. Mallis, R. J., Hamann, M. J., Zhao, W., Zhang, T., Hendrich, S., and Thomas, J. A. (2002) Irreversible thiol oxidation in carbonic anhydrase III: protection by S-glutathiolation and detection in aging rats, *Biol. Chem.* 383, 649–662.
37. Mallis, R. J., Buss, J. E., and Thomas, J. A. (2001) Oxidative modification of H-ras: S-thiolation and S-nitrosylation of reactive cysteines, *Biochem. J.* 355, 145–153.
38. Carballal, S., Radi, R., Kirk, M. C., Barnes, S., Freeman, B. A., and Alvarez, B. (2003) Sulfenic acid formation in human serum albumin by hydrogen peroxide and peroxynitrite, *Biochemistry* 42, 9906–9914.
39. Claiborne, A., Mallett, T. C., Yeh, J. I., Luba, J., and Parsonage, D. (2001) Structural, redox, and mechanistic parameters for cysteine-sulfenic acid function in catalysis and regulation, *Adv. Protein Chem.* 58, 215–276.
40. Saurin, A. T., Neubert, H., Brennan, J. P., and Eaton, P. (2004) Widespread sulfenic acid formation in tissues in response to hydrogen peroxide, *Proc. Natl. Acad. Sci. U.S.A.* 101, 17982–17987.
41. Rhee, K. Y., Erdjument-Bromage, H., Tempst, P., and Nathan, C. F. (2005) S-nitroso proteome of *Mycobacterium tuberculosis*: Enzymes of intermediary metabolism and antioxidant defense, *Proc. Natl. Acad. Sci. U.S.A.* 102, 467–472.
42. Shishebor, M. H., and Hazen, S. L. (2004) Inflammatory and oxidative markers in atherosclerosis: relationship to outcome, *Curr. Atheroscler. Rep.* 6, 243–250.

43. Viridis, A., Neves, M. F., Amiri, F., Touyz, R. M., and Schiffrin, E. L. (2004) Role of NAD(P)H oxidase on vascular alterations in angiotensin II-infused mice, *J. Hypertens.* 22, 535–542.
44. Floyd, R. A., and Hensley, K. (2002) Oxidative stress in brain aging. Implications for therapeutics of neurodegenerative diseases, *Neurobiol. Aging* 23, 795–807.
45. Klaunig, J. E., and Kamendulis, L. M. (2004) The role of oxidative stress in carcinogenesis, *Annu. Rev. Pharmacol. Toxicol.* 44, 239–267.
46. Qureshi, G. A., Baig, S., Sarwar, M., and Parvez, S. H. (2004) Neurotoxicity, oxidative stress and cerebrovascular disorders, *Neurotoxicology* 25, 121–138.
47. Lountos, G. T., Riebel, B. R., Wellborn, W. B., Bommarius, A. S., and Orville, A. M. (2004) Crystallization and preliminary analysis of a water-forming NADH oxidase from *Lactobacillus sanfranciscensis*, *Acta Crystallogr. D60*, 2044–2047.
48. Vagin, A. A., and Isupov, M. N. (2001) Spherically averaged phased translation function and its application to the search for molecules and fragments in electron-density maps, *Acta Crystallogr. D57*, 1451–1456.
49. Murshudov, G. N., Vagin, A. A., and Dodson, E. J. (1997) Refinement of macromolecular structures by the maximum-likelihood method, *Acta Crystallogr. D53*, 240–255.
50. Brünger, A. T., Adams, P. D., Clore, G. M., DeLano, W. L., Gros, P., Grosse-Kunstleve, R. W., Jiang, J. S., Kuszewski, J., Nilges, M., Pannu, N. S., Read, R. J., Rice, L. M., Simonson, T., and Warren, G. L. (1998) Crystallography & NMR system: A new software suite for macromolecular structure determination, *Acta Crystallogr. D54*, 905–921.
51. Kleywegt, G. J., and Jones, T. A. (1997) Model building and refinement practice, *Methods Enzymol.* 277, 208–230.
52. Jones, T. A., and Kjeldgaard, M. (1997) Electron-density map interpretation, *Methods Enzymol.* 277, 173–208.
53. CCP4. (1994) The CCP4 suite: Programs for protein crystallography, *Acta Crystallogr. D50*, 760–763.
54. Tickle, I. J., Laskowski, R. A., and Moss, D. S. (1998) Rfree and the Rfree ratio. I. Derivation of expected values of cross-validation residuals used in macromolecular least-squares refinement, *Acta Crystallogr. D54*, 547–557.
55. Tickle, I. J., Laskowski, R. A., and Moss, D. S. (2000) Rfree and the Rfree ratio. II. Calculation of the expected values and variances of cross-validation statistics in macromolecular least-squares refinement, *Acta Crystallogr. D56*, 442–450.
56. Read, R. J. (1997) Model phases: Probabilities and bias, *Methods Enzymol.* 277, 110–128.
57. Lamzin, V. S., and Wilson, K. S. (1993) Automated refinement of protein models, *Acta Crystallogr. D49*, 129–147.
58. Laskowski, R. A., Moss, D. S., and Thornton, J. M. (1993) Main-chain bond lengths and bond angles in protein structures, *J. Mol. Biol.* 231, 1049–1067.
59. Morris, A. L., MacArthur, M. W., Hutchinson, E. G., and Thornton, J. M. (1992) Stereochemical quality of protein structure coordinates, *Proteins* 12, 345–364.
60. Guex, N., and Peitsch, M. C. (1997) SWISS-MODEL and the Swiss-PdbViewer: an environment for comparative protein modeling, *Electrophoresis* 18, 2714–2723.
61. Pedretti, A., Villa, L., and Vistoli, G. (2004) Vega-An open platform to develop chemo-bio-informatics applications, using plug-in architecture and script programming, *J. Comput.-Aided Mol. Des.* 18, 167–173.
62. Schüttelkopf, A. W., and van Aalten, D. M. (2004) PRODRG: a tool for high-throughput crystallography of protein–ligand complexes, *Acta Crystallogr. D60*, 1355–1363.
63. Kabsch, W., and Sander, C. (1983) Dictionary of protein secondary structure: pattern recognition of hydrogen-bonded and geometrical features, *Biopolymers* 22, 2577–2637.
64. Krissinel, E., and Henrick, K. (2004) Secondary-structure matching (SSM), a new tool for fast protein structure alignment in three dimensions, *Acta Crystallogr. D60*, 2256–2268.
65. Jiang, R., and Bommarius, A. S. (2004) Hydrogen peroxide-producing NADH oxidase (nox-1) from *Lactococcus lactis*, *Tetrahedron: Asymmetry* 15, 2939–2944.
66. Schwede, T., Kopp, J., Guex, N., and Peitsch, M. C. (2003) SWISS-MODEL: An automated protein homology-modeling server, *Nucleic Acids Res.* 31, 3381–3385.
67. Wierenga, R. K., Terpstra, P., and Hol, W. G. (1986) Prediction of the occurrence of the ADP-binding beta alpha beta-fold in proteins, using an amino acid sequence fingerprint, *J. Mol. Biol.* 187, 101–107.
68. Lesk, A. M. (1995) NAD-binding domains of dehydrogenases, *Curr. Opin. Struct. Biol.* 5, 775–783.
69. Carugo, O., and Argos, P. (1997) NADP-dependent enzymes. I: Conserved stereochemistry of cofactor binding, *Proteins* 28, 10–28.
70. Karplus, P. A., and Schulz, G. E. (1989) Substrate binding and catalysis by glutathione reductase as derived from refined enzyme: substrate crystal structures at 2 Å resolution, *J. Mol. Biol.* 210, 163–180.
71. Crane, E. J., III, Parsonage, D., and Claiborne, A. (1996) The active-site histidine-10 of enterococcal NADH peroxidase is not essential for catalytic activity, *Biochemistry* 35, 2380–2387.
72. Stehle, T., Claiborne, A., and Schulz, G. E. (1993) NADH binding site and catalysis of NADH peroxidase, *Eur. J. Biochem.* 211, 221–226.
73. Parsonage, D., and Claiborne, A. (1995) Analysis of the kinetic and redox properties of NADH peroxidase C42S and C42A mutants lacking the cysteine-sulfenic acid redox center, *Biochemistry* 34, 435–441.
74. Schmidt, H. L., Stocklein, W., Danzer, J., Kirch, P., and Limbach, B. (1986) Isolation and properties of an H₂O-forming NADH oxidase from *Streptococcus faecalis*, *Eur. J. Biochem.* 156, 149–155.

BI060692P